

## Electronic Supplementary Information (ESI)

### Hygroscopic Photothermal Beads from Marine Polysaccharides: Demonstration of Efficient Atmospheric Water Production, Indoor Humidity Control and Photovoltaic Panel Cooling

Jintao He,<sup>a</sup> Na Li,<sup>a</sup> Shuxue Wang,<sup>a</sup> Shuai Li,<sup>a</sup> Chuanfei Wang,<sup>a</sup> Liangmin Yu,<sup>b,c</sup> Petri Murto<sup>\*,d</sup>  
& Xiaofeng Xu<sup>\*,a</sup>

<sup>a</sup> College of Materials Science and Engineering, Ocean University of China, Qingdao 266100, China.

<sup>b</sup> Key Laboratory of Marine Chemistry Theory and Technology, Ministry of Education, Ocean University of China, Qingdao 266100, China.

<sup>c</sup> Open Studio for Marine Corrosion and Protection, Pilot National Laboratory for Marine Science and Technology, Qingdao 266237, China.

<sup>d</sup> Department of Chemistry, University of Cambridge, Cambridge CB2 1EW, United Kingdom.

\* Corresponding authors: X. Xu, email: xuxiaofeng@ouc.edu.cn

P. Murto, email: pm707@cam.ac.uk

## Table of Contents

1. Materials .....	S3
2. Material characterization .....	S3
3. Sol–gel transition of KC .....	S4
4. Mechanical properties.....	S4
5. Gel morphologies.....	S5
6. Pore size distribution of KPL beads .....	S6
7. BJH and BET measurements .....	S7
8. FTIR measurements.....	S7
9. XPS spectra.....	S8
10. Moisture sorption measurements .....	S8
11. Raman measurements .....	S9
12. SEM and EDS of recycled KPL beads .....	S9
13. Summary of reported AWGs .....	S10
14. Sol and gel states of KC and SA.....	S11
15. Dynamic rheological properties.....	S11
16. SEM images of SPL gels .....	S12
17. Molecular dynamics (MD) simulation details. ....	S12
18. IR images of KPL beads .....	S13
19. Solar-powered evaporation measurements .....	S13
20. Calculation of solar-to-vapor conversion efficiencies .....	S13
21. Outdoor measurements .....	S14
22. Photovoltaic performance characterization .....	S15
23. Reference .....	S16

## **1. Materials**

$\kappa$ -Carrageenan (KC, >99%) and sodium alginate (SA,  $\geq$  98%) were purchased from Beijing MREDA Technology Co., Ltd. Pyrrole (>99%), lithium chloride (LiCl, 98%) and calcium chloride (CaCl<sub>2</sub>, 99%) were purchased from Sinopharm Chemical Reagent Co., Ltd.

## **2. Material characterization**

Morphology and elemental mapping were characterized by a scanning electron microscope (VEGA3, TESCAN) in combination with energy dispersive X-ray spectrometry. The UV–Vis–NIR absorption spectra were recorded with LAMBDA 1050+ spectrometer equipped with an integrating sphere. Dynamic mechanical properties were measured by a rheometer (HAAKE, MARS60). FTIR spectra were measured via a FTIR spectrometer (iS50 FTIR, Thermo Fisher Scientific). Hydrogen bonding of water in KPL hydrogels was characterized using Raman spectroscopy (alpha300, WITec). BJH pore-size distribution analysis was carried out via a surface area analyzer (ASAP2460, Micromeritics). XPS spectra were characterized via a Kratos AXIS Supra XPS spectrometer. Compressive stress–strain curves of gels were measured via a mechanical testing system equipped with a digital force gauge (M5-100, MARK-10) and a force test stand (ESM303, MARK-10). The quality of purified water was checked via an inductively coupled plasma mass spectrometry (ICP-MS, Thermo ICAP PRO).

### 3. Sol–gel transition of KC

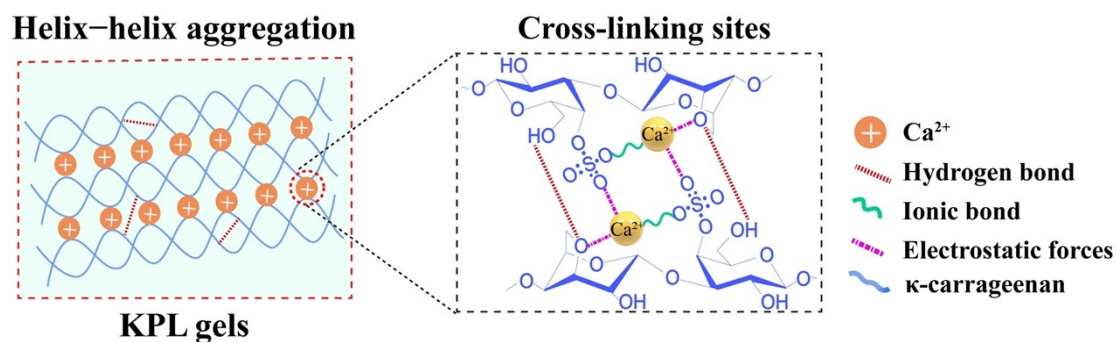


**Figure S1.** Gelation mechanism of KC in the presence of Ca<sup>2+</sup>.

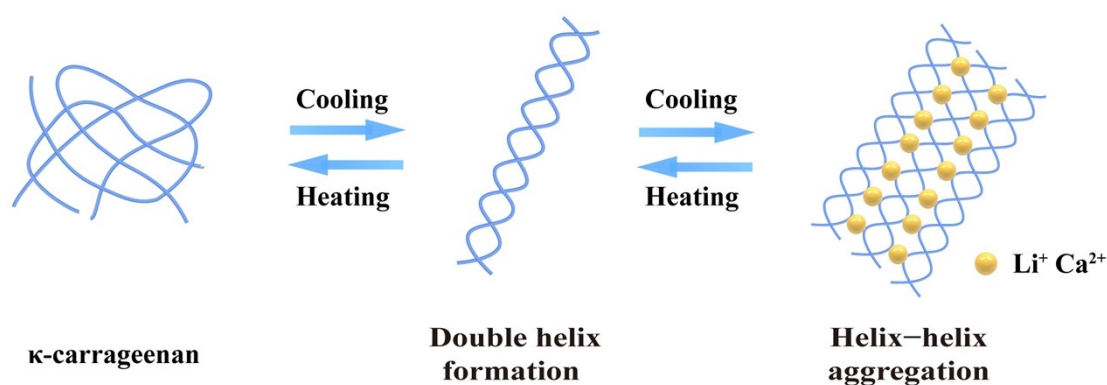


**Figure S2.** Schematic illustration of the sol–gel transition of KC in the presence of selected cations.

### 4. Mechanical properties

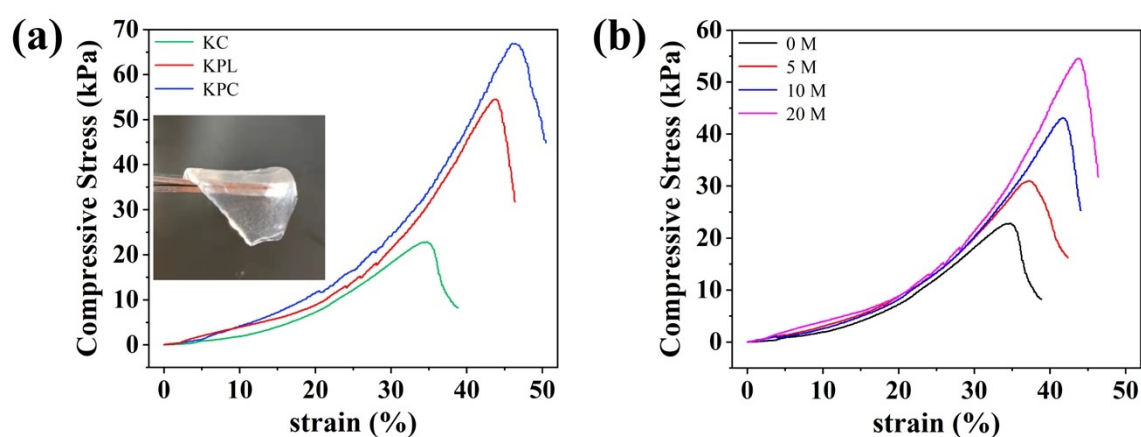


**Figure S3.** Compression stress–strain curves of (a) KC, KPL and KPC gels (The inset shows a neat KC gel); (b) Compression stress–strain curves of KC gels crosslinked in different Li<sup>+</sup> solutions (concentration: 0–20 M in water).

## 5. Gel morphologies

**Table S1.** Gel morphologies measured from different processing methods.

gel names	vacuum oven	warm oven
neat KC	irregular shape	irregular shape
KPL	hollow sphere	shrunken disk
KPL-10	shrunken sphere	shrunken disk
KPC	solid sphere	shrunken disk
SPL	soild disk	solid disk

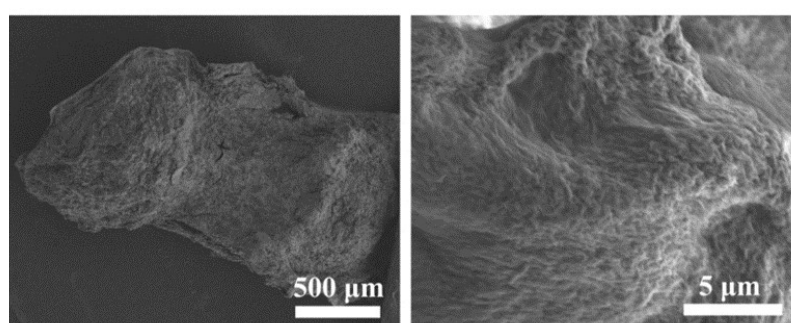


**Figure S4.** SEM images of neat KC gels.

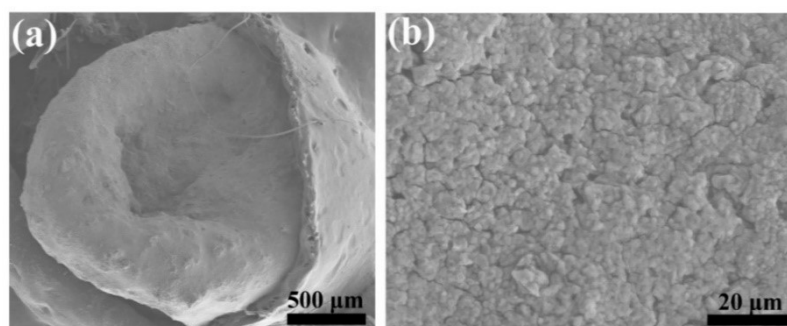


**Figure S5.** SEM images of KPL-10 gels.

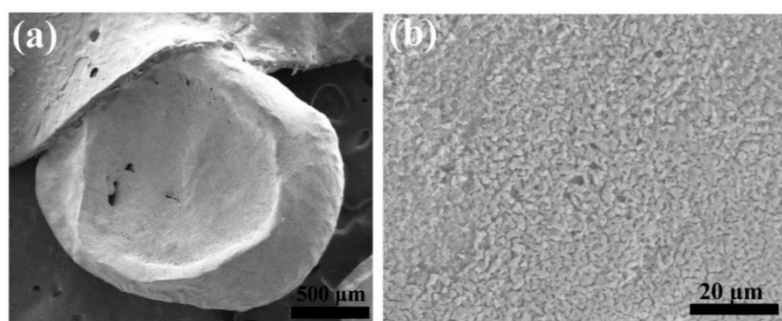


**Figure S6.** SEM images of KPC gels.

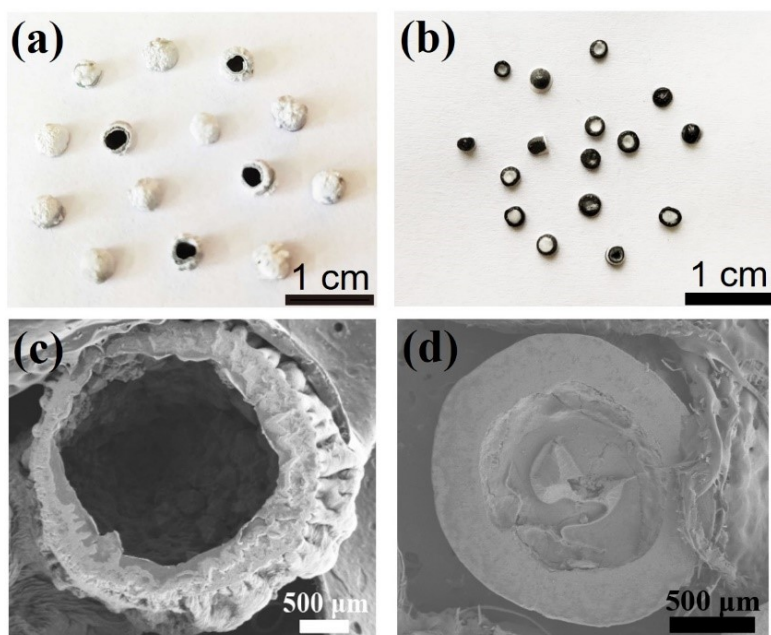


**Figure S7.** Digital photographs of KPL beads dried in (a) a vacuum oven and (b) a warm oven. Corresponding SEM images of KPL beads dried in (c) a vacuum oven and (d) a warm oven.

## 6. Pore size distribution of KPL beads

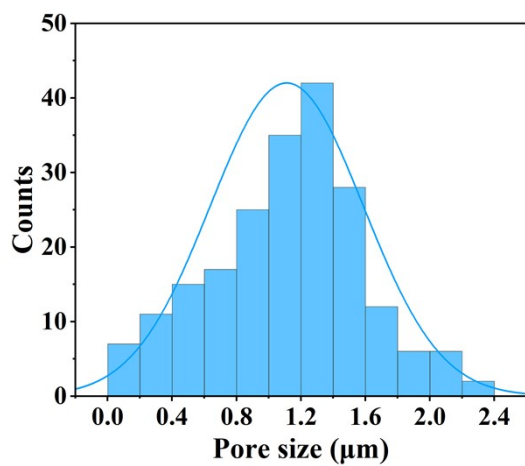


**Figure S8.** Pore size statistical distribution histograms of the porous shells of KPL beads.

## 7. BJH and BET measurements

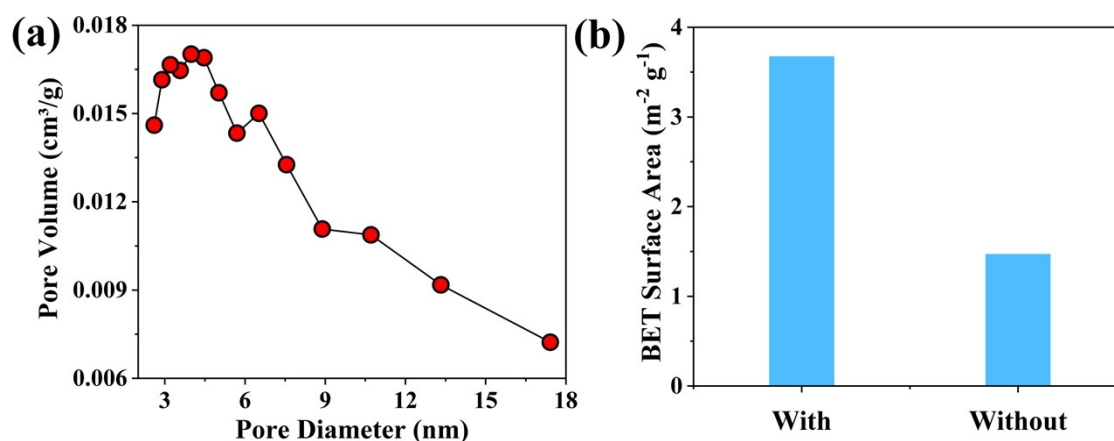


**Figure S9.** (a) BJH pore size distribution and (b) BET surface areas of KPL beads with and without hollow structures.

## 8. FTIR measurements

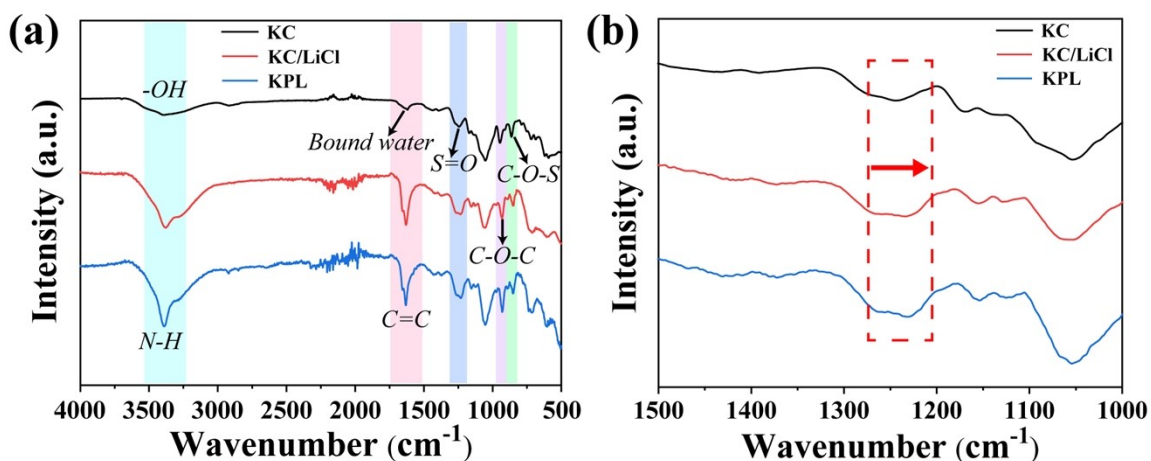


**Figure S10.** (a) FTIR spectra of neat KC, KC/LiCl and KPL and (b) zoom-in views of FTIR spectra.

## 9. XPS spectra

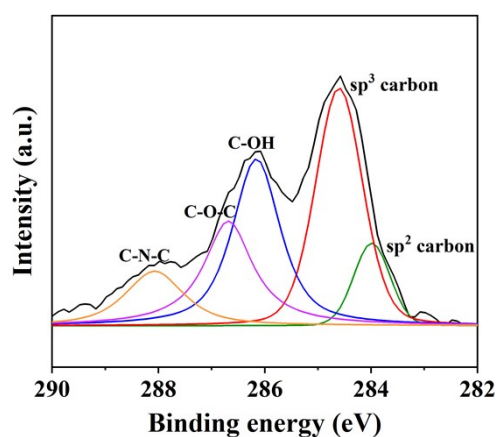


Figure S11. High-resolution XPS spectra for C 1s of KPL beads.

## 10. Moisture sorption measurements

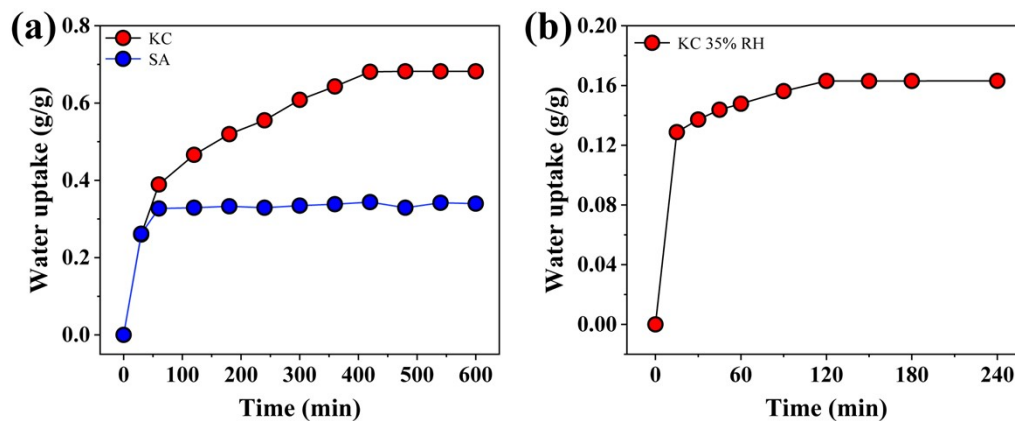


Figure S12. Water vapor sorption of (a) neat KC and SA powder under 90% RH; (b) Water vapor sorption of neat KC powder under 35% RH.

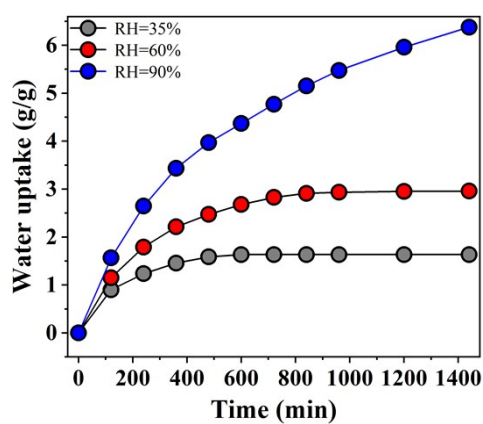
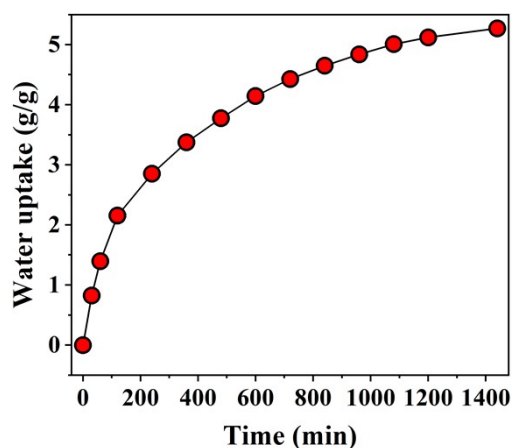
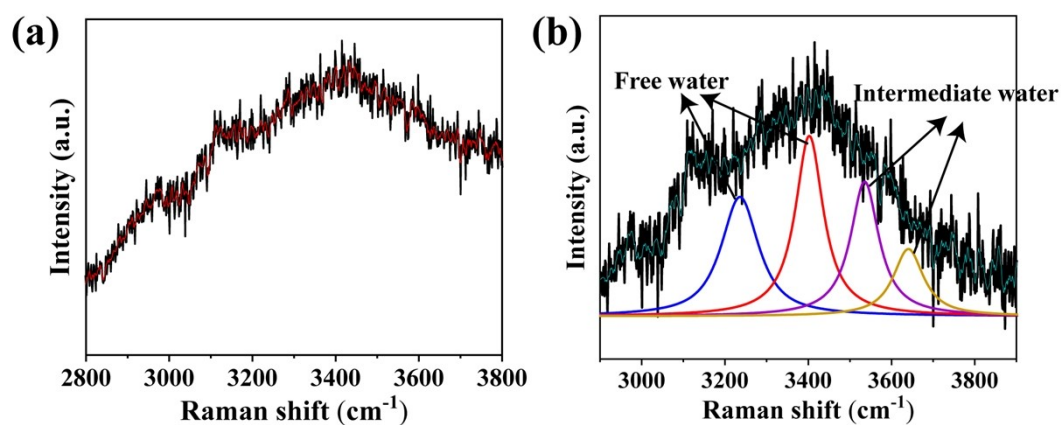


Figure S13. Water vapor sorption of LiCl powder under 35, 60 and 90% RH.



**Figure S14.** Water vapor sorption of solid KPL beads under 90% RH.

## 11. Raman spectroscopy



**Figure S15.** (a) Raman spectrum of hydrated KPL beads and (b) corresponding fitting curves in the energy region of O–H stretching modes.

## 12. SEM and EDS of recycled KPL beads

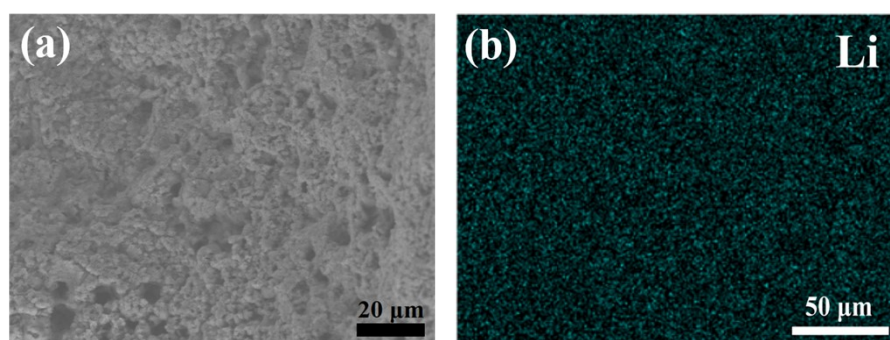


**Figure S16.** (a) SEM image and (b) elemental mapping of KPL beads after ten moisture sorption–desorption cycles.

## 13. Summary of reported AWGs

**Table S2.** Summary of sorbent-based AWGs reported in literature.

AWGs	RH/water uptake (g/g)	solar-driven water production
PAETA–Ac <sup>[1]</sup>	80%/0.87	yes
	30%/0.31	
NBHA <sup>[2]</sup>	95%/2.36	yes
	35%/0.30	
NFM <sup>[3]</sup>	90%/3.01	yes
	80%/2.72	
	60%/1.03	
PCA-MOF <sup>[4]</sup>	90%/6.39	no
	60%/1.30	
Bina/FCNT <sup>[5]</sup>	70%/5.60	no
	20%/1.40	
BCS <sup>[6]</sup>	80%/1.84	yes
	60%/1.20	
	20%/0.46	
HCS-LiCl <sup>[7]</sup>	80%/2.20	yes
	60%/1.12	
	35%/0.70	
HEPF <sup>[8]</sup>	100%/1.88	yes
	60%/1.15	
	40%/1.04	
SMAGs <sup>[9]</sup>	90%/6.70	yes
	60%/3.40	
	30%/0.70	
PGF <sup>[10]</sup>	100%/5.20	yes
	60%/0.64	
	15%/0.14	
ACF/LiCl <sup>[11]</sup>	70%/2.90	no
	20%/1.20	
PAM-CNT-CaCl <sub>2</sub> <sup>[12]</sup>	80%/1.73	yes
	60%/1.10	
	35%/0.69	
MOF-801 <sup>[13]</sup>	40%/0.28	no
	30%/0.25	
Ni <sub>2</sub> Cl <sub>2</sub> BTDD <sup>[14]</sup>	32%/1.07	no
Cr-soc-MOF-1 <sup>[15]</sup>	70%/1.95	no
Zn hydrogel <sup>[16]</sup>	90%/2.3	no

#### 14. Sol and gel states of KC and SA

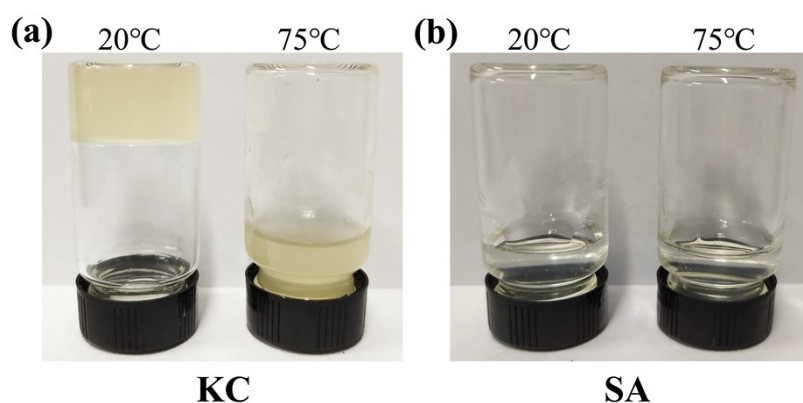


**Figure S17.** Digital photographs of (a) KC and (b) SA aqueous solutions (2 wt%) at different temperature (KC solutions showed a solid-like gel and a fluid-like gel at 20 and 75°C, respectively, while SA solutions showed fluid-like gels at low and high temperature)

#### 15. Dynamic rheological properties

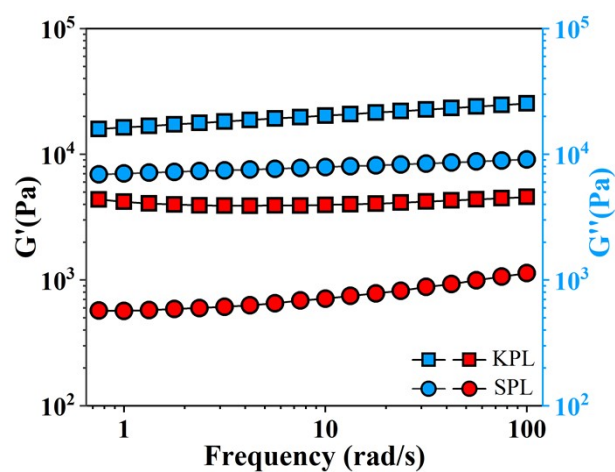


**Figure S18.**  $G'$  and  $G''$  of KPL and SPL gels under frequency sweep.

## 16. SEM images of SPL gels

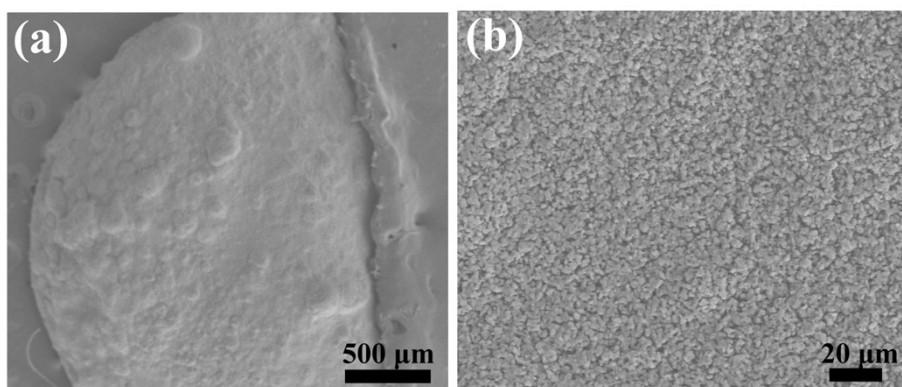


**Figure S19.** SEM images of SPL gels prepared through vacuum drying.

## 17. Molecular dynamics (MD) simulation details.

MD simulation was performed by using Gromacs 2020.4. GAFF force field was used in the calculation of organics. The atomic charge uses the RESP charge, and the total system charge was balanced with Li ions. A model consisted of 20 chains and 300 water molecules was constructed in a cubic simulation cell. System equilibration was performed in the NPT ensemble at 298.15 K and 1 atm, employing the Nose-Hoover thermostat and Berendsen barostat. The simulation was carried out for 10 ns with a time step of 2 fs in the NVT ensemble at temperatures at 298.15 K. All interactions were controlled within a cutoff radius of 1.05 nm. For the electrostatic and van der Waals interactions, the Particle-Mesh-Ewald (PME) method was used.

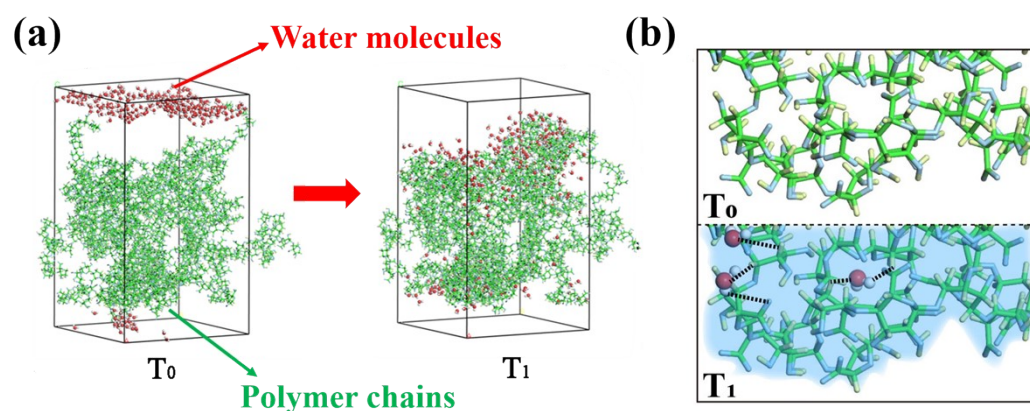


**Figure S20.** (a) MD simulation of water diffusion and (b) magnified images of water bonding in the SA matrix (Black dotted lines represent hydrogen bonds).

## 18. IR images of KPL beads

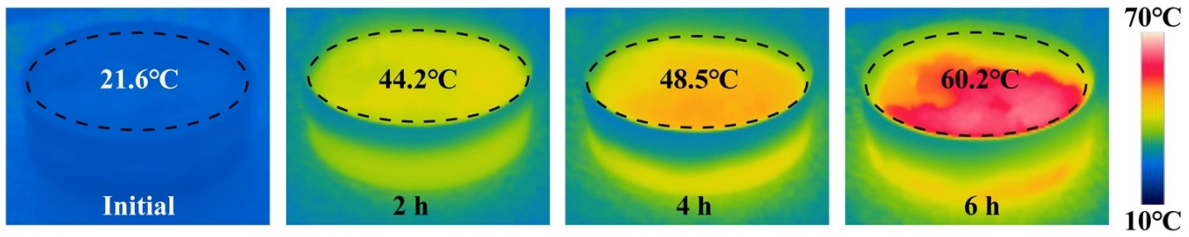


Figure S21. IR images of dry KPL beads under one sun.

## 19. Solar-powered evaporation measurements

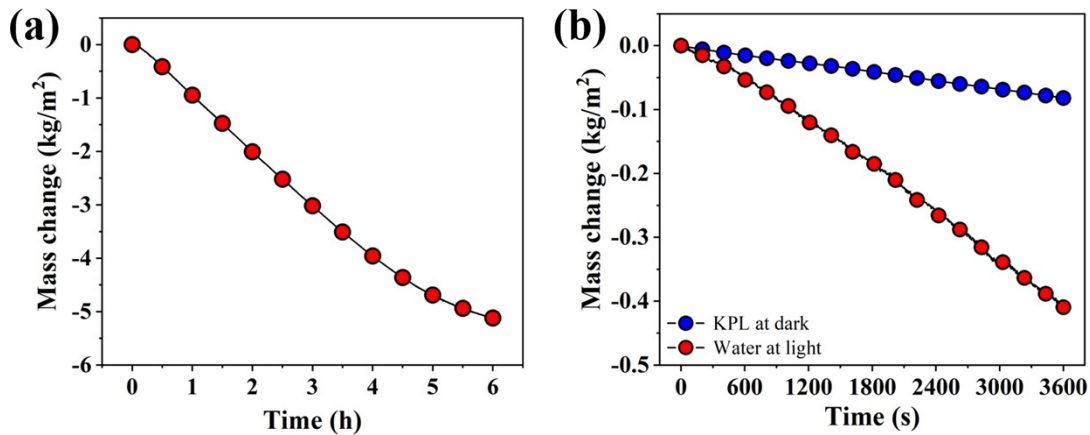


Figure S22. Mass changes of (a) water-saturated KPL beads (b) bare water over time.

## 20. Calculation of solar-to-vapor conversion efficiencies

Based on the previous reports, the solar-to-vapor efficiency was calculated using equation S1.<sup>[17]</sup>

$$\eta = \frac{\Delta m h_{lv}}{P_{in}} \quad (S1)$$

$\Delta m$  is the net evaporation rate,  $h_{lv}$  is the total enthalpy of sensible heat and phase change of liquid to water ( $2450 \text{ J g}^{-1}$ ),  $P_{in}$  is the power of the incident simulated sunlight beam ( $1 \text{ KW m}^{-2}$ ).

In our experimental,  $\Delta m = 0.94 \text{ kg m}^{-2} \text{ h}^{-1}$ . Therefore, based on the equation S1, we can calculate that the solar-to-vapor conversion efficiency of the KPL beads is 62%.

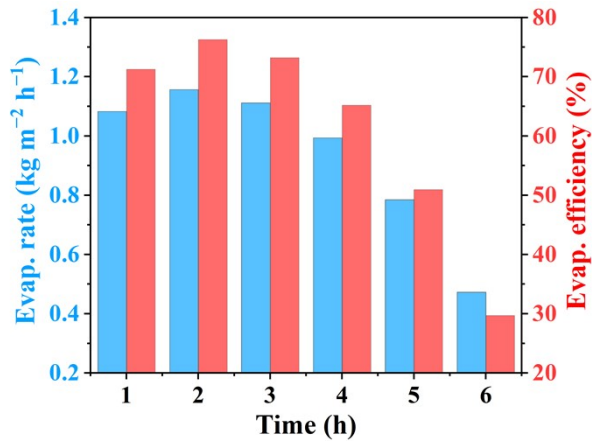


Figure S23. Water evaporation rates and solar-thermal efficiencies of KPL beads.

## 21. Outdoor measurements

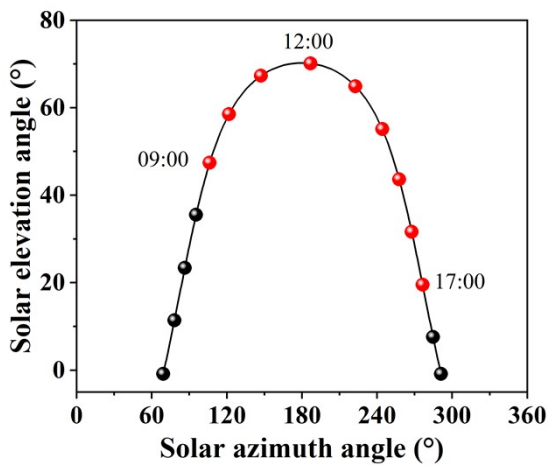


Figure S24. The Sun's position on the sky dome.

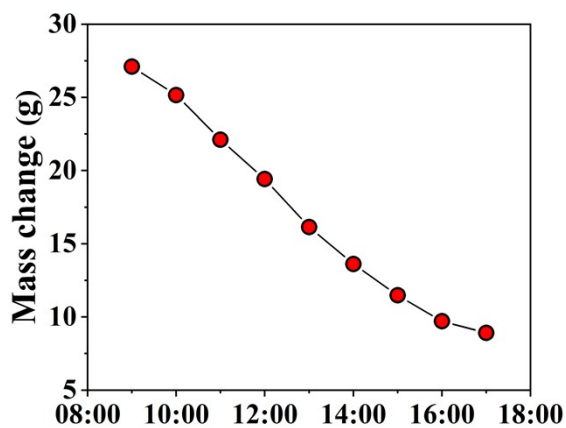


Figure S25. Mass changes of water-saturated KPL beads during outdoor evaporation measurements.

## 22. Photovoltaic performance characterization

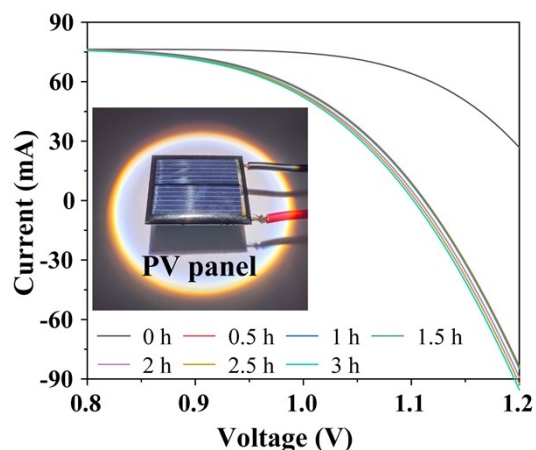


Figure S26.  $J-V$  curves of PV panels without integration of AWGs.

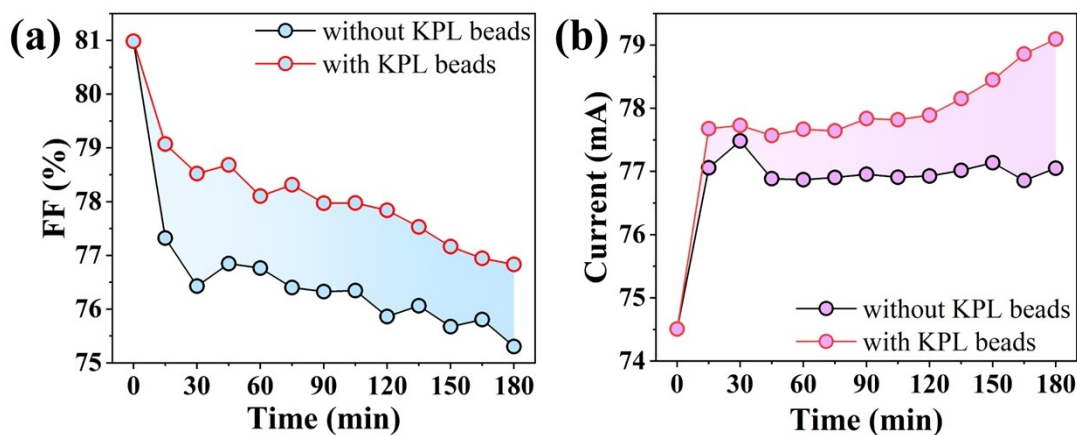


Figure S27. Variations of (a) FF and (b) photocurrent of PV panels with and without AWGs over time.

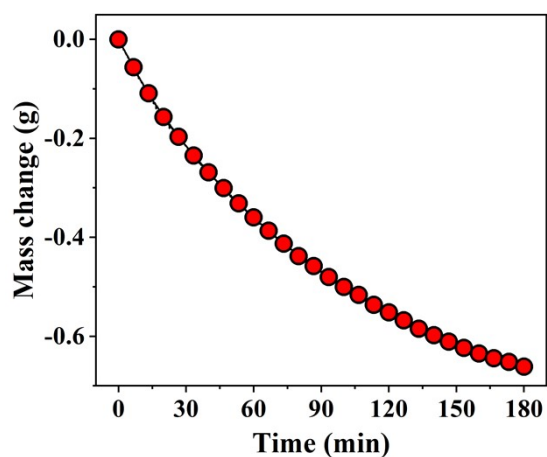


Figure S28. Mass changes of water-saturated KPL beads during photovoltaic measurements.

## 23. Reference

- [1] M. Wu, R. Li, Y. Shi, M. Altunkaya, S. Aleid, C. Zhang, W. Wang, P. Wang, *Mater. Horiz.* **2021**, 8, 1518.
- [2] M. Wang, T. Sun, D. Wan, M. Dai, S. Ling, J. Wang, Y. Liu, Y. Fang, S. Xu, J. Yeo, H. Yu, S. Liu, Q. Wang, J. Li, Y. Yang, Z. Fan, W. Chen, *Nano Energy* **2021**, 80, 105569.
- [3] Y. Zhang, L. Wu, X. Wang, J. Yu, B. Ding, *Nat. Commun.* **2020**, 11, 3302.
- [4] G. Yilmaz, F. L. Meng, W. Lu, J. Abed, C. K. N. Peh, M. Gao, E. H. Sargent, G. W. Ho, *Sci. Adv.* **2020**, 6, eabc8605.
- [5] A. Entezari, M. Ejeian, R. Wang, *ACS Mater. Lett.* **2020**, 2, 471.
- [6] F. Gong, H. Li, Q. Zhou, M. Wang, W. Wang, Y. Lv, R. Xiao, D. V. Papavassiliou, *Nano Energy* **2020**, 74, 104922.
- [7] R. Li, Y. Shi, M. Wu, S. Hong, P. Wang, *Nano Energy* **2020**, 67, 104255.
- [8] S. L. Loo, L. Vasquez, U. C. Paul, L. Campagnolo, A. Athanassiou, D. Fragouli, *ACS Appl. Mater. Interfaces* **2020**, 12, 10307.
- [9] F. Zhao, X. Zhou, Y. Liu, Y. Shi, Y. Dai, G. Yu, *Adv. Mater.* **2019**, 31, e1806446.
- [10] H. Yao, P. Zhang, Y. Huang, H. Cheng, C. Li, L. Qu, *Adv. Mater.* **2020**, 32, e1905875.
- [11] A. Entezari, M. Ejeian, R. Z. Wang, *Materials Today Energy* **2019**, 13, 362.
- [12] R. Li, Y. Shi, M. Alsaedi, M. Wu, L. Shi, P. Wang, *Environ. Sci. Technol.* **2018**, 52, 11367.
- [13] H. Kim, S. R. Rao, E. A. Kapustin, L. Zhao, S. Yang, O. M. Yaghi, E. N. Wang, *Nat. Commun.* **2018**, 9, 1191.
- [14] A. J. Rieth, A. M. Wright, G. Skorupskii, J. L. Mancuso, C. H. Hendon, M. Dinca, *J. Am. Chem. Soc.* **2019**, 141, 13858.
- [15] S. M. Towsif Abtab, D. Alezi, P. M. Bhatt, A. Shkurenko, Y. Belmabkhout, H. Aggarwal, Ł. J. Weseliński, N. Alsadun, U. Samin, M. N. Hedhili, M. Eddaoudi, *Chem* **2018**, 4, 94.
- [16] D. K. Nandakumar, S. K. Ravi, Y. Zhang, N. Guo, C. Zhang, S. C. Tan, *Energy Environ. Sci.* **2018**, 11, 2179.
- [17] Q. Jiang, L. Tian, K. K. Liu, S. Tadepalli, R. Raliya, P. Biswas, R. R. Naik, S. Singamaneni, *Adv. Mater.* **2016**, 28, 9400.